frontiers
in Energy Research

ORIGINAL RESEARCH
published: 02 December 2021
doi: 10.3389/fenrg.2021.780473

A Kernel for Calculating PEM Fuel Cell Distribution of Relaxation Times

Andrei Kulikovsky *

Forschungszentrum Jülich GmbH, Theory and Computation of Energy Materials (IEK–13), Institute of Energy and Climate Research, Jülich, Germany

Impedance of all oxygen transport processes in PEM fuel cell has negative real part in some frequency domain. A kernel for calculation of distribution of relaxation times (DRT) of a PEM fuel cell is suggested. The kernel is designed for capturing impedance with negative real part and it stems from the equation for impedance of oxygen transport through the gas-diffusion transport layer (doi:10.1149/2.0911509jes). Using recent analytical solution for the cell impedance, it is shown that DRT calculated with the novel K_2 kernel correctly captures the GDL transport peak, whereas the classic DRT based on the *RC*-circuit (Debye) kernel misses this peak. Using K_2 kernel, analysis of DRT spectra of a real PEMFC is performed. The leftmost on the frequency scale DRT peak represents oxygen transport in the channel, and the rightmost peak is due to proton transport in the cathode catalyst layer. The second, third, and fourth peaks exhibit oxygen transport in the GDL, faradaic reactions on the cathode side, and oxygen transport in the catalyst layer, respectively.

Keywords: PEM fuel cell, impedance, GDL, modeling, distribution of relaxation times (DRT)

Edited by:
Quentin Meyer,
University of New South Wales,
Australia

Reviewed by:
Yoed Tsur,
Technion Israel Institute of Technology, Israel
Hao Yuan,
Tongji University, China

Correspondence:
Andrei Kulikovsky
a.kulikovsky@fz-juelich.de

Specialty section:
This article was submitted to Fuel Cells,
a section of the journal
Frontiers in Energy Research

Received: *21 September 2021*
Accepted: *19 October 2021*
Published: *02 December 2021*

Citation:
Kulikovsky A (2021) A Kernel for Calculating PEM Fuel Cell Distribution of Relaxation Times.
Front. Energy Res. 9:780473.
doi: 10.3389/fenrg.2021.780473

1 INTRODUCTION

Electrochemical impedance spectroscopy provides unique opportunity for testing and characterization of PEM fuel cells without interruption of current production mode (Lasia, 2014). A classic approach to interpretation of EIS data is construction of equivalent electric circuit having impedance spectrum close to the measured one. However, a more attractive option provides the distribution of relaxation times (DRT) technique. Note that DRT is sometimes called distribution function of relaxation times.

In the context of PEM fuel cell studies, the idea of DRT can be explained as follows. To a first approximation, PEM fuel cell impedance Z can be modeled as impedance of a parallel RC circuit

$$Z = \frac{R}{1 + \mathrm{i}\omega RC}, \tag{1}$$

where ω is the angular frequency of applied AC signal. This approximation corresponds to the cell with ideal (fast) transport of reactants in all transport media (Kulikovsky, 2017). In that case, R describes Tafel resistivity of the oxygen reduction reaction (ORR), and C represents the superficial double-layer capacitance of the electrode.

In general, to calculate transport contributions to cell impedance, one has to develop a transport model for the ORR reactants. However, if information on transport resistivities and characteristic frequencies suffices, DRT provides a simpler option. Denoting $RC = \tau$, multiplying the right side of **Eq. 1** by nonnegative function $\gamma(\tau)$ and integrating over τ, we get

$$Z(\omega) = R_{pol}\int_0^{\infty}\frac{\gamma(\tau)d\tau}{1+\mathrm{i}\omega\tau} \tag{2}$$

where R_{pol} is the total polarization resistivity of the cell, and the function γ is the DRT of impedance Z. Mathematically, **Eq. 2** means expansion of $Z(\omega)$ into infinite sum of RC impedances, with the resistivity of each elementary RC circuit being $R_{pol}\gamma\, d\tau$. The function

$$K_{RC}(\omega,\tau) = \frac{1}{1+\mathrm{i}\omega\tau} \tag{3}$$

under integral in **Eq. 2** is usually called "Debye model" (Barsoukov and Macdonald, 2018). **Eq. 2** can also be considered as integral transform of $\gamma(\tau)$, which justifies the term "*RC* kernel" for **Eq. 3**.

Quite evidently, DRT of a single parallel RC circuit is Dirac delta function $\gamma = \delta(\tau - \tau_*)$ positioned at $\tau_* = RC$. This example illustrates the main feature of DRT: it converts any RC-like impedance into a single, more or less smeared on the τ scale δ-like peak.

All transport processes in a fuel cell eventually are linked to the double-layer capacitance in the catalyst layer; thus, it is usually assumed that impedance of every process is not far from impedance of a parallel RC circuit. That means that the DRT of a PEMFC is expected to consist of several delta-like peaks. As the regular frequency $f = 1/(2\pi\tau)$, it is convenient to plot $\gamma(f)$ instead of $\gamma(\tau)$. Position of each $\gamma(f)$ peak marks a characteristic frequency of the respective transport process and

$$R_n = R_{pol}\int_{\tau_n}^{\tau_{n+1}}\gamma(\tau)\,d\tau \tag{4}$$

gives the contribution of process resistivity to the total cell polarization resistivity R_{pol}. Here, τ_n and τ_{n+1} are the peak boundaries on the τ scale.

Fuel cell impedance is usually measured on equidistant in log-scale frequency mesh $\{f_n, n = 1, \ldots, N\}$, with $\ln(f_{n+1}) - \ln(f_n)$ being independent of n. From numerical perspective, it is beneficial to deal with the function $G(\tau)$ satisfying to

$$Z(\omega) = R_{\infty} + R_{pol}\int_{-\infty}^{\infty}\frac{G(\tau)\,d\ln(\tau)}{1+\mathrm{i}\omega\tau}, \tag{5}$$

where the term R_{∞} is added to describe pure ohmic (high-frequency) fuel cell resistivity. Clearly, $\gamma = G/\tau$, and **Eq. 4** in terms of G takes the form

$$\begin{aligned} R_n &= R_{pol}\int_{\tau_n}^{\tau_{n+1}} G(\tau)\,d\ln\tau \\ &= 2\pi R_{pol}\int_{f_n}^{f_{n+1}} G(f)\,d\ln(f), \quad f_n < f_{n+1} \end{aligned} \tag{6}$$

where the frequencies $f_n = 1/(2\pi\tau_{n+1})$ and $f_{n+1} = 1/(2\pi\tau_n)$ mark the peak boundaries. Note that **Eqs 4**, **6** return a single peak resistivity if the DRT peaks are not overlapped; otherwise, R_n would represent the sum of overlapped peak resistivities. The problem of overlapped peak resistivity is alleviated if the DRT in analytical form is found, as in, for example, the ISGP method (Avioz Cohen et al., 2021).

Setting in **Eq. 5** $\omega = 0$ and taking into account that $Z(0) - R_{\infty} = R_{pol}$, we see that G obeys to normalization condition

$$\int_{-\infty}^{\infty} G(\tau)\,d\ln\tau = 2\pi\int_{-\infty}^{\infty} G(f)\,d\ln f = 1 \tag{7}$$

In the following, **Eq. 5** will be discussed, as G is usually used instead of γ in practical calculations.

DRT technique, **Eq. 2**, was invented by Fuoss and Kirkwood (1941) in the context of polymer materials impedance and brought to the fuel cell community seemingly by Schichlein et al. (2002). Since 2002, a lot of works from the group of Ivers–Tiffée have been devoted to deciphering of solid oxide fuel cell spectra by means of DRT [see a review (Ivers-Tiffee and Weber, 2017)]. Analysis of PEMFC impedance spectra using DRT is a relatively new field (Heinzmann et al., 2018; Avioz Cohen et al., 2021; Reshetenko and Kulikovsky, 2021; Wang et al., 2021). Heinzmann et al. (2018) measured impedance spectra of a small (1 cm^2) laboratory PEMFC and studied DRT peak behavior depending on cell temperature, relative humidity (RH), oxygen concentration, and current density. They obtained DRT with up to five peaks; the leftmost on the frequency scale peak P1 was attributed to oxygen diffusion in the gas-diffusion and cathode catalyst layers (CCLs). Avioz Cohen et al. (2021) performed impedance measurements of a 5-cm^2 cell varying temperature, RH, and current density. The calculated DRT consisted of four peaks, attributed (in ascending frequencies) to (1) oxygen transport in the GDL/CCL, (2) ORR, (3) proton transport in the CCL, and (4) proton transport in membrane. Note that Heinzmann et al. and Cohen et al. used different codes for DRT calculation. Wang et al. (2021) measured impedance spectra of application-relevant 25-cm^2 PEMFC and obtained a three–peak DRT; the lowest frequency peak was attributed to oxygen diffusion processes in the cell. In our recent work (Reshetenko and Kulikovsky, 2021), DRT spectra of a low-Pt PEMFC have been reported; we attributed the low-frequency peak to oxygen transport in the GDL and, possibly, in the channel.

In PEMFCs, the supplied oxygen (air) is transported through the four quite different media: channel, GDL, open pores of the CCL, and finally through Nafion film covering Pt/C agglomerates. One therefore could expect four corresponding peaks in the DRT spectra. However, in Heinzmann et al. (2018), Avioz Cohen et al. (2021), and Wang et al. (2021), a single oxygen transport peak has been reported. There are two options to explain this result: either some of the oxygen transport peaks overlap with each other (or with the ORR peak) and DRT is not able to separate them, or the codes used were unable to resolve all the transport processes. It is important to note that the code for DRT calculation of Wan et al. (2015) used in Heinzmann et al. (2018) and Wang et al. (2021), the ISGP code (Hershkovitz et al., 2011) used in Avioz Cohen et al. (2021), and our code using Tikhonov regularization (Tikhonov, 1995) in combination with NNLS solver (Kulikovsky, 2020a; Kulikovsky, 2021a) are based on the RC kernel, **Eq. 5**.

The real part of RC-circuit impedance, **Eq. 1**, is positive, and the imaginary part is negative. This imposes limits on functions Z,

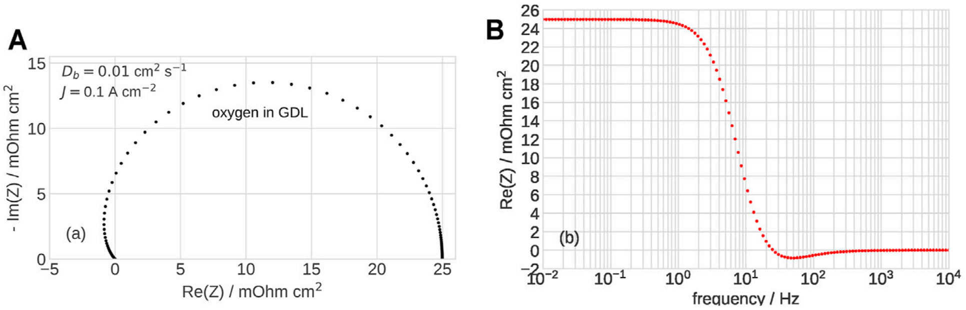

FIGURE 1 | (A) Nyquist spectrum of the gas-diffusion layer impedance, **Eq. 10**. **(B)** Frequency dependence of the real part of impedance in **(A)**. Parameters for calculations are listed in **Table 1**.

which could be represented by **Eq. 5**. For example, impedance of an inductive loop cannot be expanded in infinite series of *RC* impedances, as the imaginary part of inductive impedance is positive. Quite similarly, the impedance *Z* having negative real part in some frequency domain also cannot be represented by **Eq. 5**.

Below, we show that the DRT calculated with *RC* kernel could completely miss some of the transport peaks in PEMFC spectra. An alternative K_2 kernel better capturing oxygen transport processes in the cell cathode is suggested. The kernel is illustrated by calculation of DRT of the recent analytical PEM fuel cell impedance spectrum (Kulikovsky, 2021b). Finally, we show that the new kernel well separates the channel, GDL, and ORR peaks in the DRT spectra of a standard Pt/C-based PEM fuel cell.

2 MODEL: K_2 KERNEL

Below, the following dimensionless variables will be used

$$\tilde{c} = \frac{c}{c_h^{in}}, \quad \tilde{J} = \frac{J}{i_* l_t}, \quad \tilde{\eta} = \frac{\eta}{b}, \quad \tilde{D}_b = \frac{4FD_b c_h^{in}}{i_* l_t^2}, \quad \tilde{l}_b = \frac{l_b}{l_t}, \\ \tilde{\omega} = \omega t_*, \quad \tilde{Z} = \frac{Z i_* l_t}{b}. \tag{8}$$

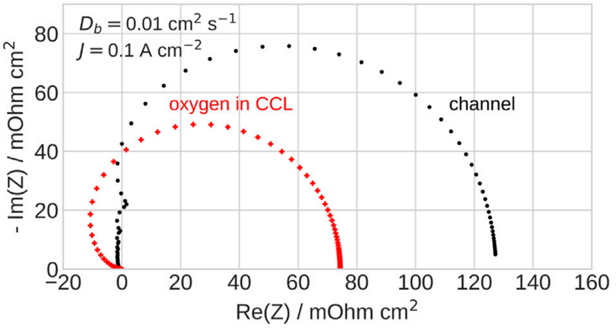

FIGURE 2 | Nyquist spectra of the channel impedance, **Appendix Eq. A1** and of impedance of oxygen transport in the CCL (Kulikovsky, 2017).

Here, t_* is the characteristic time of double-layer charging

$$t_* = \frac{C_{dl} b}{i_*}, \tag{9}$$

c is the oxygen concentration, c_h^{in} is the reference oxygen concentration, C_{dl} is the volumetric double-layer capacitance, J is the mean current density in the cell, η is the ORR overpotential, positive by convention, b is the ORR Tafel slope, i_* is the volumetric ORR exchange current density, l_t is the CCL thickness, D_b is the oxygen diffusion coefficient in the GDL, and l_b is the GDL thickness.

Analytical GDL impedance $\tilde{Z}_{gdl}$ has been derived in Kulikovsky and Shamardina (2015). For the cell current densities well below the limiting current density due to oxygen transport in the GDL, $\tilde{Z}_{gdl}$ has the form

$$\tilde{Z}_{gdl} = \frac{\tanh\left(\mu \tilde{l}_b \sqrt{i\tilde{\omega}/\tilde{D}_b}\right)}{\mu \sqrt{i\tilde{\omega}\tilde{D}_b}\left(1 + i\tilde{\omega}/\tilde{J}\right)} \tag{10}$$

where μ is the constant parameter

$$\mu = \sqrt{\frac{4Fc_h^{in}}{C_{dl} b}}, \tag{11}$$

Eq. 10 has been obtained from the general expression for the cathode side impedance in the limit of infinite air flow stoichiometry (Kulikovsky and Shamardina, 2015). **Eq. 10** is a Warburg finite-length impedance divided by the factor $(1 + i\tilde{\omega}/\tilde{J})$. The factor describes the effect of double-layer charging by the cell current density $\tilde{J}$ transported in the form of oxygen flux through the GDL to the attached CCL (Kulikovsky and Shamardina, 2015). In his classic work (Warburg, 1899), Warburg used static polarization curve to derive the boundary condition for calculation of transport impedance of a semi-infinite electrode [**Eq. 4** of Ref. (Warburg, 1899)]. Later, Warburg model was extended for the case of finite-length transport layer, using the same boundary condition on the electrode side [see Lasia (2014), page 104]. However, account of capacitive term in the electrode charge conservation equation changes the boundary condition for the oxygen transport equation (Kulikovsky and Shamardina, 2015), leading to the

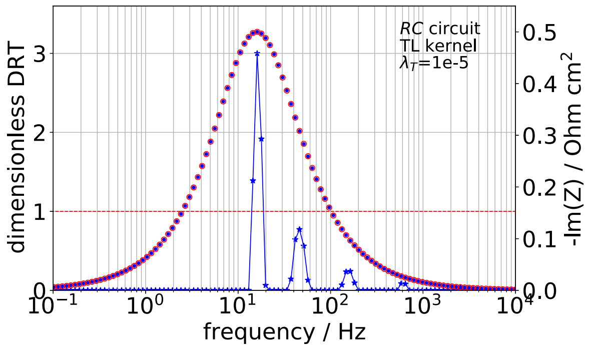

FIGURE 3 | DRT (solid line, blue stars, left axis) and imaginary part of *RC*-circuit impedance 1/(1 + 10^{-2}iω) (blue dots, right axis) calculated with **Eq. 16** and α = 1 for all frequencies. Open red circles show imaginary part reconstructed from the calculated DRT using **Eq. 16**. Dashed red line plots α = 1 for this calculation.

additional factor $(1 + \mathrm{i}\tilde{\omega}/\tilde{J})$ in the denominator of **Eq. 10**. Nyquist plot of impedance (10) is shown in **Figure 1A**; frequency dependence of $\mathrm{Re}(\tilde{Z}_{gdl})$ is depicted in **Figure 1B**. As can be seen, between 20 and 200 Hz, the real part of Z_{gdl} is essentially negative, and at higher frequencies $\mathrm{Re}(\tilde{Z}_{gdl})$ tends to zero. As the real part of Warburg finite-length impedance is positive, the negative real part of impedance (10) is due to the term $(1 + \mathrm{i}\tilde{\omega}/\tilde{J})$ in the denominator.

Impedance of oxygen transport in channel, **Appendix Eq. A1**, and in the CCL (Kulikovsky, 2017) also exhibits negative real part (**Figure 2**). Last but not least, in low-Pt cells, an important role plays oxygen transport through a thin Nafion film covering Pt/C agglomerates in the CCL (Greszler et al., 2012; Weber and Kusoglu, 2014; Kongkanand and Mathias, 2016). The spectrum of this transport layer is quite similar in shape to the spectrum in **Figure 1** (Kulikovsky, 2021a). Thus, all the oxygen transport processes in a PEMFC cannot be described by the standard *RC* kernel, and another kernel suitable for description of impedance elements with the negative real part is needed.

In a standard PEMFC, unless the cell current density is small, the DRT peaks of oxygen transport in the GDL, CCL, and channel are expected to locate at frequencies below the frequency f_{ct} of faradaic (charge transfer) processes. Thus, to capture the oxygen transport peaks, correction for the negative real part of impedance is needed in the range of frequencies $f < f_{ct}$. The kernel K_2 suggested in his work consists, thus, of two parts:

$$K_2 = \begin{cases} \dfrac{\tanh\sqrt{\mathrm{i}\omega\tau}}{\sqrt{\mathrm{i}\omega\tau}\,(1 + \mathrm{i}\omega\tau)}, & f \le f_*, \quad \text{TL kernel} \\[2ex] \dfrac{1}{1 + \mathrm{i}\omega\tau}, & f > f_*, \quad \textit{RC kernel} \end{cases} \tag{12}$$

where $f_* \simeq f_{ct}$ is the threshold frequency. Selection of optimal f_* is discussed below. A function similar to impedance of a transport layer (TL) (10) forms the low-frequency part of K_2; the real part of this function is negative at $\omega\tau > 1.81052$. The high-frequency (*RC*) part of K_2 is the standard *RC*-circuit kernel. Switching between TL and *RC* kernels is necessary, as the TL part itself does not describe well *RC*-circuit impedance (see below). The real part of GDL impedance becomes negative at ≃20 Hz (**Figure 1B**),

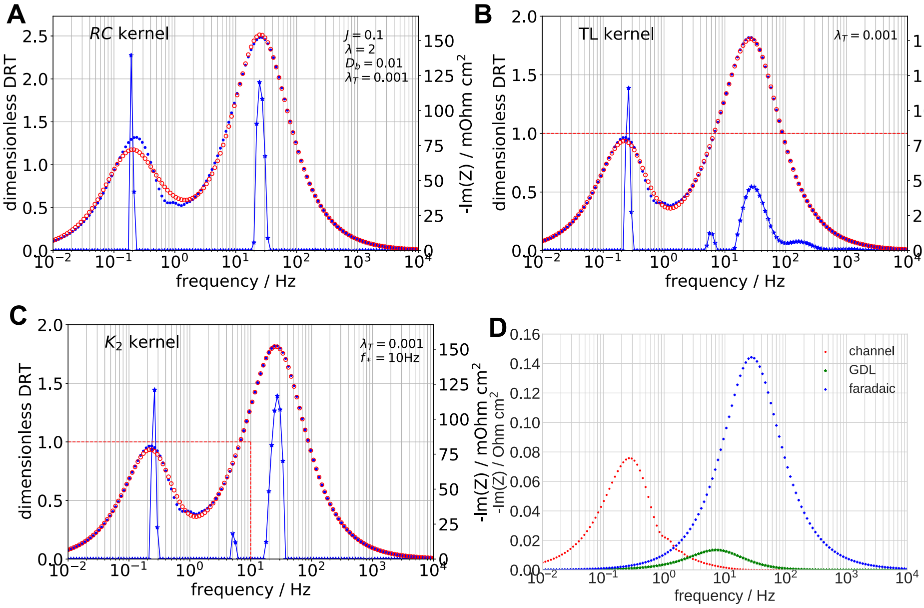

FIGURE 4 | (A) DRT calculated with the *RC* kernel (solid line, left axis) using imaginary part of the total cathode side impedance, **Appendix Eq. A6** (blue dots, right axis). Red open circles—$\mathrm{Im}(Z_{tot})$ reconstructed from the calculated DRT. **(B)** The same as in **(A)** curves obtained with the *TL* kernel (α = 1) over the whole frequency range. Red dashed line indicates the plot of α function, **Eq. 14**. **(C)** The curves as in **(A)** obtained with the K_2 kernel and threshold frequency f_* = 10 Hz. (**D**) Separate imaginary parts of the channel, GDL, and faradaic impedance.

TABLE 1 | The base–case cell parameters used in calculations.

GDL thickness l_b, cm	0.023
Catalyst layer thickness l_t, cm	10×10^{-4} (10 μm)
ORR Tafel slope b, mV	30
Double-layer capacitance C_{dl}, F cm^{-3}	20
GDL oxygen diffusivity D_b, cm^2 s^{-1}	0.01
Cell current density J, A cm^{-2}	0.1
Pressure	Standard
Cell temperature T, K	273 + 80
Air flow stoichiometry λ	2.0

TABLE 2 | Channel, GDL, and faradaic resistivities (Ω cm^2) resulting from DRT, **Eq. 6**. Star $*$ indicates the value calculated as a sum of faradaic and all high-frequency peaks in **Figure 4B**. The first row shows exact data calculated with **Appendix Eqs. A13**.

	Channel	GDL	Faradaic
Exact	0.127	0.0250	0.300
RC kernel	0.140	—	0.308
TL kernel	0.125	0.0185	0.304*
K_2 kernel	0.125	0.0171	0.305

TABLE 3 | PEM fuel cell geometric and operating parameters.

GDL thickness l_b, cm	0.023
Catalyst layer thickness l_t, cm	12×10^{-4} (12 μm)
Cell active area, cm^2	76
Absolute cathode pressure, kPa	150
Cathode flow RH	50%
Cell temperature T, K	273 + 80
H$_2$/air flow stoichiometry λ	2/2

while the imaginary part at this frequency is quite large (**Figure 1A**). This shape of impedance around and below 20 Hz is thus far from the *RC*-circuit impedance and the TL kernel is needed to "recognize" this shape. At higher frequencies, transport impedances tend to zero, and the Debye kernel works better. The idea behind **Eq. 12** is thus to expand the low-frequency components of cell impedance using the TL kernel and the high-frequency components using the standard *RC* kernel.

It is convenient to combine **Eq. 12** into one function

$$K_2 = \frac{\tanh\left(\alpha\sqrt{i\omega\tau}\right)}{\alpha\sqrt{i\omega\tau}\,(1 + i\omega\tau)} \tag{13}$$

where α is a step function of the frequency f

$$\alpha = 1 - H\left(f - f_*\right) + \epsilon, \tag{14}$$

$H(x)$ is the Heaviside step function, and $\epsilon = 10^{-10}$ is a small parameter to avoid zero division error. Parameter α therefore changes from 1 to 0 at the threshold frequency $f = f_*$. With $\alpha \to 0$, the Warburg factor in **Eq. 13** tends to unity:

$$\frac{\tanh\left(\alpha\sqrt{i\omega\tau}\right)}{\alpha\sqrt{i\omega\tau}} \to 1, \quad \text{as} \quad \alpha \to 0 \tag{15}$$

and hence the α function serves as a switch between the two kernels in **Eq. 12**.

With **Eq. 13**, **5** takes the form

$$Z = R_\infty + R_{pol}\int_{-\infty}^{\infty} \frac{\tanh\left(\alpha\sqrt{i\omega\tau}\right) G(\tau)\, d\ln(\tau)}{\alpha\sqrt{i\omega\tau}\,(1 + i\omega\tau)}. \tag{16}$$

Setting in **Eq. 16** $\omega \to 0$, it is easy to show that G still obeys to normalization conditions, **Eq. 7**.

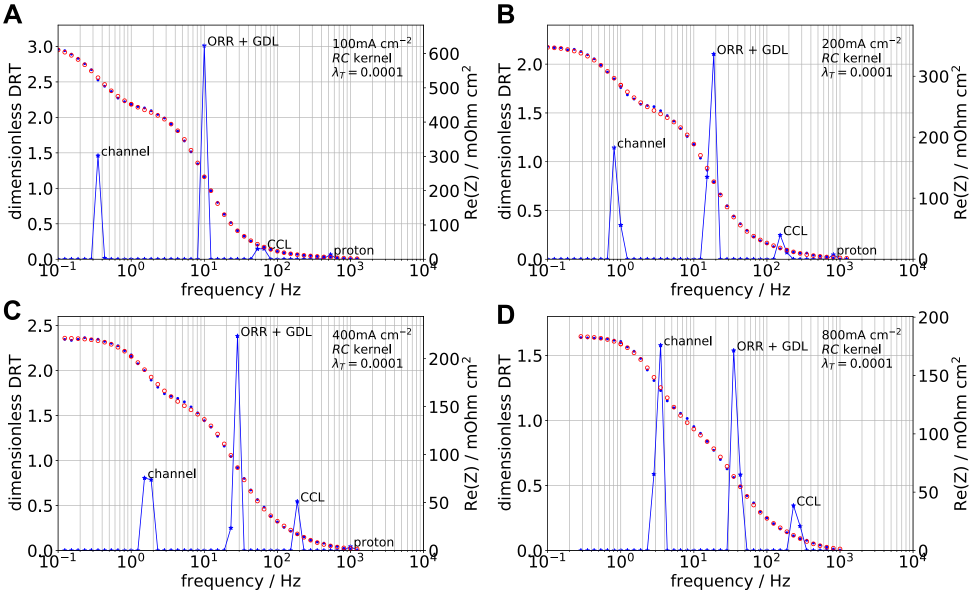

FIGURE 5 | DRT (solid line, left axis) calculated with the *RC* kernel using real part of the experimental PEMFC impedance (blue dots, right axis) for the current densities **(A)** 100, **(B)** 200, **(C)** 400, and **(D)** 800 mA cm^{-2}. Red open circles—Re(Z) reconstructed from the calculated DRT.

3 NUMERICAL RESULTS AND DISCUSSION

3.1 Synthetic Impedance Tests

Figure 3 shows the imaginary part of the *RC*-circuit impedance for $R = 1$, $C = 0.01$ and the DRT calculated using **Eq. 16**, and $\alpha = 1$ for all frequencies (TL kernel). As can be seen, the main peak is positioned correctly at the frequency $1/(2\pi RC)$; however, the DRT spectrum exhibits three phantom peaks located to the right of the main peak. It is worth noting that quite similarly, the *RC* kernel generates several phantom peaks in the DRT of Warburg finite-length impedance (Kulikovsky, 2020a), that is, no single kernel is able to correctly represent DRT of all impedance components.

In a standard PEMFC, the characteristic frequencies of channel and GDL impedance are approximately 1 and 10 Hz, respectively (Kulikovsky, 2021b). Thus, the typical value of the threshold frequency f_* in **Eq. 14** should be about 10 Hz; however, the exact value can always be selected simply looking at the calculated DRT spectrum. In standard PEMFCs operated at oxygen stoichiometry of 2, the faradaic DRT peak is located to the right of the GDL transport peak on the log-frequency scale (see below).

Analytical impedance $\tilde{Z}_{tot}$ of the PEMFC cathode side has been obtained in Kulikovsky (2021b), assuming fast proton and oxygen transport in the CCL. Equation for $\tilde{Z}_{tot}$ includes three components: impedance $\tilde{Z}_{chan}$ due to oxygen transport in channel, impedance $\tilde{Z}_{gdl}$ of oxygen transport in the GDL, and faradaic (charge–transfer) impedance $\tilde{Z}_{ct}$ The respective formulas are listed in the Appendix; these solutions allow us to check how well DRT from **Eq. 16** captures the channel, GDL, and faradaic components in the total impedance $\tilde{Z}_{tot}$ spectrum (**Figure 4**).

The spectrum of $\tilde{Z}_{tot}$ has been calculated in the frequency range of 10^{-2} to 10^{4} Hz with 22 points per decade. Parameters for impedance calculation are listed in **Table 1**. **Figure 4D** depicts the imaginary part of the impedance components calculated using equations in the Appendix. Imaginary part of $\tilde{Z}_{tot}$ has then been used for calculation of DRT using our recent algorithm based on Tikhonov's regularization and nonnegative least-squares (NNLS) solver (Kulikovsky, 2020a; Kulikovsky, 2021a). The NNLS method greatly outperforms projected gradient iterations suggested in Kulikovsky (2020a). In all the cases, the *L*-curve method (Hansen, 1992) gave the regularization parameter $\lambda_T \simeq 10^{-3}$. Variation of λ_T in the range of plus–minus order of magnitude did not change the number and position of peaks. At 10 times larger λ_T, the peaks get wider and started overlapping.

Figure 4A shows the DRT spectrum of $\tilde{Z}_{tot}$, **Appendix Eq. A6**, calculated using the *RC* kernel. As can be seen, the standard kernel returns only two peaks corresponding to the channel (left peak) and faradaic (right peak) impedance. The GDL peak, which is clearly seen in **Figure 4D**, is completely missing. Note poor quality of reconstructed imaginary part (red open circles) between 0.1 and 20 Hz. This is a result of poor description of the cell impedance by **Eq. 5** in the frequency domain where the real part of GDL impedance is negative.

Figure 4B displays the DRT calculated with the "pure" TL kernel, **Eq. 12**. The GDL peak is resolved, and the quality of reconstructed imaginary part is much better; however, phantom high-frequency peaks to the right of the faradaic peak are clearly seen (cf. **Figure 3**). **Figure 4C** shows the DRT spectrum calculated using the K_2 kernel with the threshold frequency of 10 Hz; the GDL peak is well resolved, and the phantom peaks vanish. It is worth mentioning that the real part of the total cell impedance is always positive due to positive contributions of the faradaic and proton transport impedances. However, the Debye kernel fails to recognize the transport impedances having negative real part, as the whole shape of this impedance strongly deviates from the *RC* circuit one. The result in **Figure 4C** shows that in order to be recognized, the DRT peak corresponding to the process with negative real part must be fully "covered" by the TL kernel. The respective DRT peak frequency corresponds to the peak value of the imaginary part of impedance (cf. **Figures 4C,D**).

Table 2 shows the resistivities, **Eq. 6**, corresponding to individual peaks in **Figure 4**. As can be seen, K_2 kernel provides good estimate of the channel and faradaic resistivities; however, the GDL resistivity R_{gdl} is underestimated by 30%.

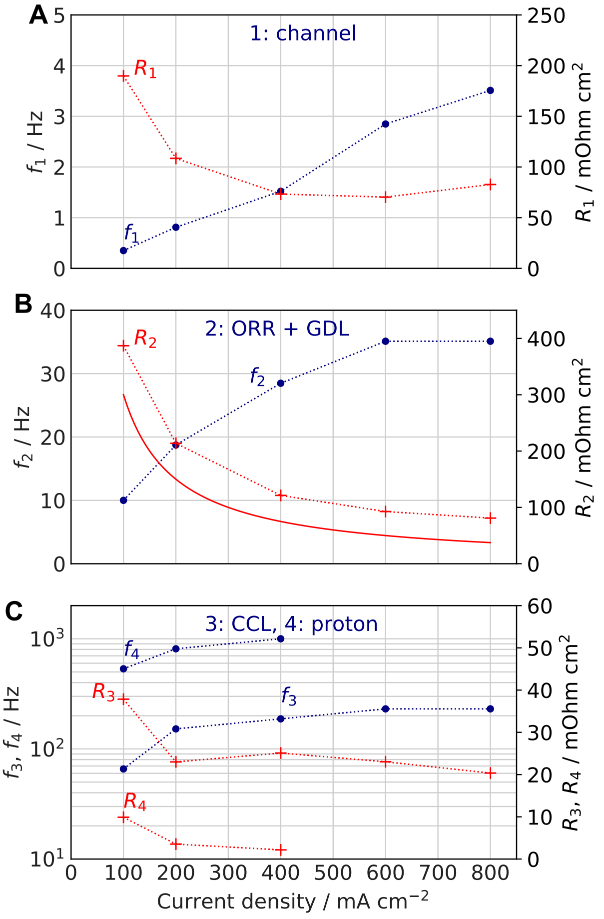

FIGURE 6 | Frequency (blue curves, left axis) and resistivity (red curves, right axis) of the DRT peaks calculated using *RC* kernel (**Figure 5**) versus mean cell current density *J*. **(A)** first peak, **(B)** second peak and **(C)** third and fourth peaks.

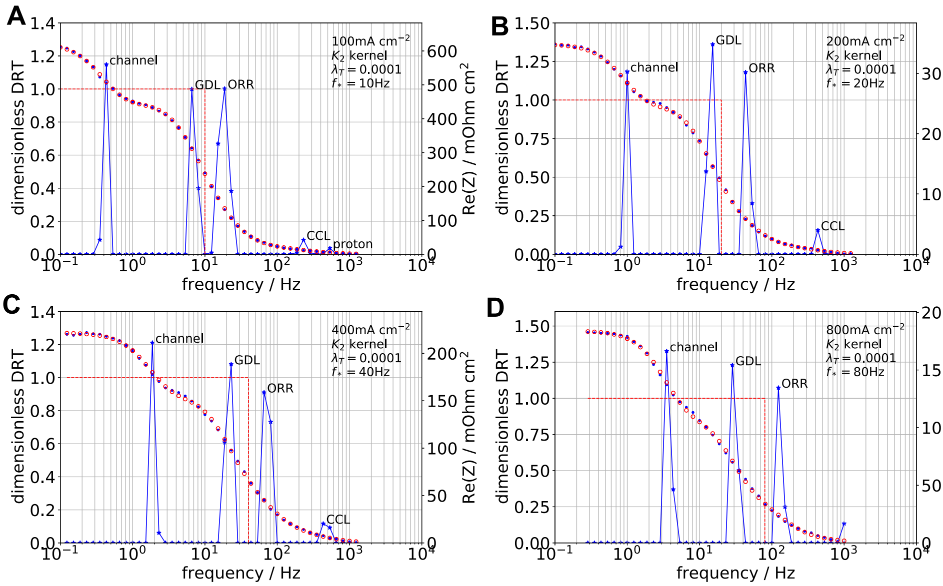

FIGURE 7 | DRT (solid line, left axis) calculated with the K_2 kernel using real part of the experimental PEMFC impedance (blue dots, right axis) for the current densities **(A)** 100, **(B)** 200, **(C)** 400, and **(D)** 800 mA cm^{-2}. Red open circles—Re(Z) reconstructed from the calculated DRT. Dashed line shows the plot of α, **Eq. 14**, switching the K_2 kernel from TL– to RC–one at the frequency marked by vertical line.

Nonetheless, as the contribution of R_{gdl} is small, the 30% accuracy could be tolerated.

3.2 Real PEMFC Spectra

A crucial check for the new kernel is calculation of DRT of a real PEM fuel cell. Impedance spectra of a standard Pt/C-based PEMFC have been measured in the frequency range of 0.1 to approximately 10^3 Hz with 11 points per decade. The cell geometrical parameters and operating conditions are listed in **Table 3**; note that the air flow stoichiometry was 2 in this set of measurements. The impedance points in the frequency range above $\simeq 10^3$ Hz have been discarded due to effect of cable inductance. More details on experimental setup and measuring procedures can be found in Reshetenko and Kulikovsky (2019).

Figure 5 shows DRT spectra calculated with the real part of measured impedance using the RC kernel. **Figure 6** shows the respective peak frequencies and resistivities. The DRT spectra in **Figures 5A–C** exhibit four peaks, whereas in **Figure 5D**, the most high-frequency peak disappears. This peak represents proton transport in the CCL, and at high cell currents, it shifts to frequencies that have been discarded. The characteristic frequency f_4 of proton transport in the CCL is given by Kulikovsky (2020b)

$$f_4 \simeq \frac{2\sigma_p}{C_{dl} l_t^2} \tag{17}$$

With the typical values of $\sigma_p \simeq 0.01$ S cm^{-1} and $C_{dl} \simeq 20$ F cm^{-3} [Ref. (Reshetenko and Kulikovsky, 2019)], we get $f_p \simeq 700$ Hz, which by the order of magnitude agrees with the proton peak position in **Figures 5A–C**. The growth of f_4 with the cell current and the respective decay of the peak resistivity R_4 (**Figure 6C**) is due to growing amount of liquid water improving the CCL proton conductivity.

The leftmost peak in **Figures 5A–D** represents impedance due to oxygen transport in the cathode channel. The characteristic frequency f_1 of this peak linearly increases with the cell current density (**Figure 6A**), which is a signature of channel impedance (Kulikovsky, 2021b).

The highest, second peak in the DRT spectra (**Figures 5A–D**) represents the contributions of ORR and oxygen transport in the GDL (see below). In the absence of strong oxygen and proton transport limitations, the ORR resistivity is given by

$$R_{ORR} = \frac{b}{J} \tag{18}$$

which follows the Tafel law. Qualitatively, the shape of second peak resistivity R_2 follows the trend of **Eq. 18** due to dominating contribution of ORR resistivity to this peak (**Figure 6B**). Note that the separate GDL peak is not resolved by the RC kernel.

The third CCL peak in **Figures 5A–D** is most probably due to oxygen transport in the CCL pores. For the estimate. we take the Warburg finite-length formula for the transport layer frequency f_W

$$f_W = \frac{2.54D}{2\pi l^2} \tag{19}$$

where D is the oxygen diffusivity in the transport layer of the thickness l. Setting $f_W = 35$ Hz (**Figure 5A**) and $l = l_t$, for the oxygen diffusion coefficient in the CCL, we get $D_{ox} \simeq 1.2 \cdot 10^{-4}$ cm^2 s^{-1}, which agrees with measurements (Reshetenko and Kulikovsky, 2019). With the growth of cell current, the

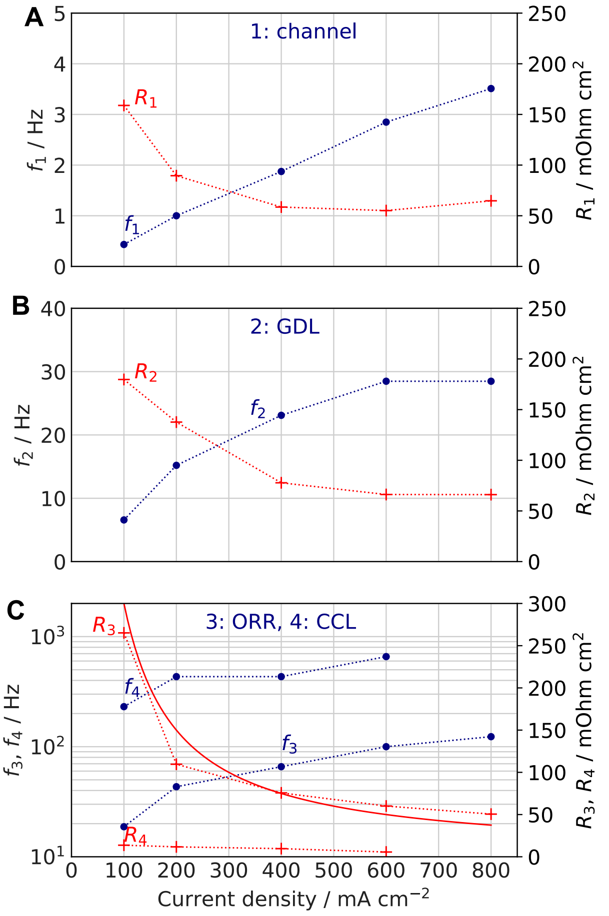

FIGURE 8 | Frequency and resistivity of the DRT peaks calculated using K_2 kernel (**Figure 7**) versus mean cell current density J. Solid line in **(C)** is the Tafel ORR resistivity $R_{ORR} = b/J$ plotted with the Tafel slope $b = 0.03$ V (69 mV/decade). **(A)** first peak, **(B)** second peak and **(C)** third and fourth peaks.

peak frequency f_3 rapidly shifts to 200 Hz (**Figure 6C**), corresponding to $D_{ox} \simeq 7 \cdot 10^{-4}$ cm^2 s^{-1}. This result correlates with the growth of D_{ox} resulting from fitting of physics-based impedance model to the PEMFC cell spectra (Reshetenko and Kulikovsky, 2016). The mechanism of this growth yet is unclear.

Figure 7 shows the DRT of the same impedance spectra calculated with the K_2 kernel. The properties of K_2 kernel are immediately seen: setting of the threshold frequency f_* in **Eq. 14** just to the left of the "ORR + GDL" peak in **Figures 5A–D** splits this peak into two well-resolved peaks (**Figures 7A–D**). The left peak of this doublet corresponds to the GDL impedance and the right peak to the ORR impedance. With the K_2 kernel, the proton transport peak is seen only at the smallest cell current density (**Figure 7A**), whereas at higher currents the peak vanishes, indicating its shift to the frequencies greater than 1 kHz (**Figures 7B–D**).

Splitting the "CCL + GDL" peak into GDL and ORR peaks is confirmed by the behavior of peak resistivities in **Figures 8B,C**, respectively. The ORR peak resistivity R_3 follows the trend of **Eq. 18** (solid line in **Figure 8C**) with the ORR Tafel slope $b = 30$ mV, which is a typical value for Pt/C cells (Neyerlin et al., 2006). The GDL resistivity R_2 decreases in the range of cell currents 100 to 400 mA cm^{-2} and remains nearly constant at higher currents (**Figure 8B**). Using again the Warburg formula **Eq. 19**, with $l = l_b = 230 \cdot 10^{-4}$ cm and the frequency between 10 and 30 Hz (**Figure 8B**), for the GDL oxygen diffusivity, we get quite reasonable values of $D_b \simeq 0.013$–0.033 cm^2 s^{-1}. The increase of D_b in the range of 100 to 400 mA cm^{-2} is probably due to growing air flow velocity in the channel at the constant stoichiometry, which facilitates liquid droplets removal from the GDL.

Comparing the GDL peaks in **Figures 7A,B** one can see that the area under this peak increases with the cell current density. However, the area under the peak gives the fraction of the respective process resistivity in the total polarization resistivity of the cell R_{pol}. The latter value decreases with the cell current, leading to decrease in the absolute value of R_{GDL} (**Figure 8B**).

K_2 kernel returns twice lower resistivity and about twice higher frequency of the CCL peak (cf. f_3, R_3 in **Figure 6C** and f_4, R_4 in **Figure 8C**). This shift leads to twice higher estimate of the CCL oxygen diffusivity, which is still acceptable (see above). Overall, confirmation of the CCL peak nature requires measurements at variable oxygen concentration and RH. An important issue is accuracy of peak resistivities calculated using the K_2 kernel. Impedance spectra fitting by physics-based model seems to be the only way to get an independent estimate of the resistivities for comparison.

Over the past years, large efforts have been directed toward development of universal code capable to calculate DRT based on *RC* kernel, not using any *a priori* information on the system [see a nice review of Effendy, Song and Bazant (Effendy et al., 2020)]. However, in PEMFC studies, it would be wasteful to ignore analytical results, showing that the *RC* kernel alone is not well suited for DRT description of the spectra.

4 CONCLUSION

Impedance of all oxygen transport processes in a PEM fuel cell exhibits negative real part in some frequency range. This makes it difficult to accurately calculate the respective DRT peaks using the standard *RC* kernel $1/(1 + i\omega\tau)$. A novel kernel K_2, **Eq. 13**, is suggested. K_2 combines the low-frequency transport layer kernel having a domain with negative real part and the standard *RC* kernel for description of faradaic and high-frequency processes in the cell. Calculation of DRT for analytical PEMFC impedance shows that K_2 kernel captures the peak due to oxygen transport in the gas-diffusion layer, whereas the *RC* kernel can miss this peak. Comparison of Pt/C PEMFC DRT calculated using *RC* and K_2 kernel shows that the K_2 kernel resolves the GDL oxygen transport peak, which otherwise is merged to the ORR peak when using the standard *RC* kernel. Overall, the K_2 spectra of a standard Pt/C PEMFC operating at the air flow stoichiometry $\lambda = 2$ consist of five peaks. In the frequency ascending order, these peaks are due to (1) oxygen transport in channel, (2) oxygen transport in the GDL, (3) faradaic reactions, (4) oxygen transport in the CCL, and (5) proton transport in the CCL. If the CCL proton conductivity is high, the peak (6) shifts to the frequencies well above 1 kHz, and it may not be resolved due to inductance of measuring system.

DATA AVAILABILITY STATEMENT

The original contributions presented in the study are included in the article/Supplementary Material, further inquiries can be directed to the corresponding author.

AUTHOR CONTRIBUTIONS

The author confirms being the sole contributor of this work and has approved it for publication.

ACKNOWLEDGMENTS

The author is grateful to Tatyana Reshetenko (University of Hawaii) for experimental spectra used in this work and useful discussions.

REFERENCES

Avioz Cohen, G., Gelman, D., and Tsur, Y. (2021). Development of a Typical Distribution Function of Relaxation Times Model for Polymer Electrolyte Membrane Fuel Cells and Quantifying the Resistance to Proton Conduction within the Catalyst Layer. *J. Phys. Chem. C* 125, 11867–11874. doi:10.1021/acs.jpcc.1c03667

Barsoukov, E., and Macdonald, J. R. (2018). *Impedance Spectroscopy: Theory, Experiment, and Applications*. 3 edition. New Jersey: John Wiley & Sons.

Effendy, S., Song, J., and Bazant, M. Z. (2020). Analysis, Design, and Generalization of Electrochemical Impedance Spectroscopy (EIS) Inversion Algorithms. *J. Electrochem. Soc.* 167, 106508. doi:10.1149/1945-7111/ab9c82

Fuoss, R. M., and Kirkwood, J. G. (1941). Electrical Properties of Solids. VIII. Dipole Moments in Polyvinyl Chloride-Diphenyl Systems*. *J. Am. Chem. Soc.* 63, 385–394. doi:10.1021/ja01847a013

Greszler, T. A., Caulk, D., and Sinha, P. (2012). The Impact of Platinum Loading on Oxygen Transport Resistance. *J. Electrochem. Soc.* 159, F831–F840. doi:10.1149/2.061212jes

Hansen, P. C. (1992). Analysis of Discrete Ill-Posed Problems by Means of the L-Curve. *SIAM Rev.* 34, 561–580. doi:10.2307/213262810.1137/1034115

Heinzmann, M., Weber, A., and Ivers-Tiffée, E. (2018). Advanced Impedance Study of Polymer Electrolyte Membrane Single Cells by Means of Distribution of Relaxation Times. *J. Power Sourc.* 402, 24–33. doi:10.1016/j.jpowsour.2018.09.004

Hershkovitz, S., Tomer, S., Baltianski, S., and Tsur, Y. (2011). Isgp: Impedance Spectroscopy Analysis Using Evolutionary Programming Procedure. *ECS Trans.* 33, 67–73. doi:10.1149/1.3589186

Ivers-Tiffee, E., and Weber, A. E. (2017). Evaluation of Electrochemical Impedance Spectra by the Distribution of Relaxation Times. *J. Ceram. Soc. Jpn.* 125, 193–201. doi:10.2109/jcersj2.16267

Kongkanand, A., and Mathias, M. F. (2016). The Priority and Challenge of High-Power Performance of Low-Platinum Proton-Exchange Membrane Fuel Cells. *J. Phys. Chem. Lett.* 7, 1127–1137. doi:10.1021/acs.jpclett.6b00216

Kulikovsky, A. A. (2017). Analytical Physics-Based Impedance of the Cathode Catalyst Layer in a PEM Fuel Cell at Typical Working Currents. *Electrochimica Acta* 225, 559–565. doi:10.1016/j.electacta.2016.11.129

Kulikovsky, A. (2020). Analysis of Proton and Electron Transport Impedance of a PEM Fuel Cell in H_2/N_2 Regime. *Electrochem. Sci. Adv.* 1, e202000023. doi:10.1002/elsa.202000023

Kulikovsky, A. (2021). Analytical Impedance of Oxygen Transport in the Channel and Gas Diffusion Layer of a PEM Fuel Cell. *J. Electrochem. Soc.* doi:10.1149/1945-7111/ac3a2d

Kulikovsky, A. (2021). Impedance and Resistivity of Low-Pt Cathode in a PEM Fuel Cell. *J. Electrochem. Soc.* 168, 044512. doi:10.1149/1945-7111/abf508

Kulikovsky, A. (2020). PEM Fuel Cell Distribution of Relaxation Times: a Method for the Calculation and Behavior of an Oxygen Transport Peak. *Phys. Chem. Chem. Phys.* 22, 19131–19138. doi:10.1039/D0CP02094J

Kulikovsky, A., and Shamardina, O. (2015). A Model for PEM Fuel Cell Impedance: Oxygen Flow in the Channel Triggers Spatial and Frequency Oscillations of the Local Impedance. *J. Electrochem. Soc.* 162, F1068–F1077. doi:10.1149/2.0911509jes

Lasia, A. (2014). *Electrochemical Impedance Spectroscopy and its Applications*. New York: Springer.

Neyerlin, K. C., Gu, W., Jorne, J., and Gasteiger, H. A. (2006). Determination of Catalyst Unique Parameters for the Oxygen Reduction Reaction in a PEMFC. *J. Electrochem. Soc.* 153, A1955–A1963. doi:10.1149/2.0471803jes10.1149/1.2266294

Reshetenko, T., and Kulikovsky, A. (2019). A Model for Local Impedance: Validation of the Model for Local Parameters Recovery from a Single Spectrum of PEM Fuel Cell. *J. Electrochem. Soc.* 166, F431–F439. doi:10.1149/2.1241906jes

Reshetenko, T., and Kulikovsky, A. (2021). Understanding the Distribution of Relaxation Times of a Low-Pt PEM Fuel Cell. *Electrochimica Acta* 391, 138954. doi:10.1016/j.electacta.2021.138954

Reshetenko, T., and Kulikovsky, A. (2016). Variation of PEM Fuel Cell Physical Parameters with Current: Impedance Spectroscopy Study. *J. Electrochem. Soc.* 163 (9), F1100–F1106. doi:10.1149/2.0981609jes

Schichlein, H., Müller, A. C., Voigts, M., Krügel, A., and Ivers-Tiffée, E. (2002). Deconvolution of Electrochemical Impedance Spectra for the Identification of Electrode Reaction Mechanisms in Solid Oxide Fuel Cells. *J. Appl. Electrochem.* 32, 875–882. doi:10.1023/A:1020599525160

Tikhonov, A. N. (1995). *Numerical Methods for the Solution of Ill-Posed Problems*. Dordrecht: Kluwer.

Wan, T. H., Saccoccio, M., Chen, C., and Ciucci, F. (2015). Influence of the Discretization Methods on the Distribution of Relaxation Times Deconvolution: Implementing Radial Basis Functions with DRTtools. *Electrochimica Acta* 184, 483–499. doi:10.1016/j.electacta.2015.09.097

Wang, Q., Hu, Z., Xu, L., Li, J., Gan, Q., Du, X., et al. (2021). A Comparative Study of Equivalent Circuit Model and Distribution of Relaxation Times for Fuel Cell Impedance Diagnosis. *Int. J. Energ. Res.* 45, 15948–15961. doi:10.1002/er.6825

Warburg, E. (1899). Ueber das Verhalten sogenannter unpolarisirbarer Elektroden gegen Wechselstrom. *Ann. Phys. Chem.* 303, 493–499. doi:10.1002/andp.18993030302

Weber, A. Z., and Kusoglu, A. (2014). Unexplained Transport Resistances for Low-Loaded Fuel-Cell Catalyst Layers. *J. Mater. Chem. A.* 2, 17207–17211. doi:10.1039/c4ta02952f

Conflict of Interest: The author declares that the research was conducted in the absence of any commercial or financial relationships that could be construed as a potential conflict of interest.

APPENDIX A. MODEL EQUATIONS FOR GDL, CHANNEL, AND FARADAIC IMPEDANCE

Equations of this section have been derived in Kulikovsky (2021b).

- Channel impedance is

$$\tilde{Z}_{chan} = -\frac{4\lambda \mathrm{e}^{\tilde{\eta}_0} N_c}{\left(2\lambda \mathrm{i}\tilde{\omega} + (2\lambda - 1)\mathrm{e}^{\tilde{\eta}_0}\right) D_c} \tag{A1}$$

where

$$\begin{aligned} N_c = {} & \lambda^2 \tilde{J}\,(\mathrm{e}^{2\tilde{\eta}_0} + (\tilde{J} + \mathrm{i}\tilde{\omega}\,(1+\xi^2))\mathrm{e}^{\tilde{\eta}_0} - \xi^2\tilde{\omega}^2)\exp\left(\frac{-\mathrm{e}^{\tilde{\eta}_0} - \mathrm{i}\tilde{\omega}\xi^2}{\lambda\tilde{J}}\right) \\ & + \lambda\left(\mathrm{e}^{\tilde{\eta}_0} - \lambda\tilde{J} + \mathrm{i}\tilde{\omega}\xi^2\right)\left(\mathrm{e}^{2\tilde{\eta}_0} + (\tilde{J} + \mathrm{i}\tilde{\omega}\,(\xi^2+1))\mathrm{e}^{\tilde{\eta}_0} - \xi^2\tilde{\omega}^2\right) - \left(\mathrm{e}^{\tilde{\eta}_0} + \mathrm{i}\tilde{\omega}\xi^2\right)^2 \mathrm{e}^{\tilde{\eta}_0}/2 \end{aligned} \tag{A2}$$

$$\begin{aligned} D_c = {} & 2\lambda^2\tilde{J}\left(\mathrm{e}^{2\tilde{\eta}_0} + (\tilde{J} + \mathrm{i}\tilde{\omega}\,(1+\xi^2))\mathrm{e}^{\tilde{\eta}_0} - \xi^2\tilde{\omega}^2\right)\exp\left(\frac{-\mathrm{e}^{\tilde{\eta}_0} - \mathrm{i}\tilde{\omega}\xi^2}{\lambda\tilde{J}}\right)\mathrm{e}^{\tilde{\eta}_0} - 2\lambda\xi^6\tilde{\omega}^4 \\ & + \mathrm{i}\left(2\lambda\xi^2 - \xi^2 + 4\lambda\right)\xi^4\mathrm{e}^{\tilde{\eta}_0}\,\tilde{\omega}^3 + 2\xi^2\left(\left(2\lambda\xi^2 - \xi^2 + \lambda\right)\mathrm{e}^{\tilde{\eta}_0} + \lambda^2\tilde{J}\right)\mathrm{e}^{\tilde{\eta}_0}\tilde{\omega}^2 \\ & - \mathrm{i}\left((2\lambda-1)\xi^2\mathrm{e}^{\tilde{\eta}_0} + 2\lambda\tilde{J}\left(\lambda\xi^2 - \xi^2 + \lambda\right)\right)\mathrm{e}^{2\tilde{\eta}_0}\tilde{\omega} - 2\lambda\tilde{J}\left((\lambda-1)\mathrm{e}^{\tilde{\eta}_0} + \lambda\tilde{J}\right)\mathrm{e}^{2\tilde{\eta}_0}. \end{aligned} \tag{A3}$$

and parameters ξ and λ are given by

$$\xi = \sqrt{\frac{4Fhc_h^{in}}{C_{dl}l_t b}}, \quad \lambda = \frac{4Fhvc_h^{in}}{LJ}. \tag{A4}$$

- GDL impedance is given by **Eq. 10**.
- Faradaic impedance is

$$\tilde{Z}_{ct} = \frac{1}{\mathrm{i}\tilde{\omega} + \left(1 - \frac{1}{2\lambda}\right)\mathrm{e}^{\tilde{\eta}_0}} \tag{A5}$$

- Total impedance of the cathode side, including channel, GDL, and faradaic components

$$\tilde{Z}_{tot} = \frac{\lambda B^3}{D_{tot}}\left(\cosh(\phi) + \frac{\mathrm{e}^{\tilde{\eta}_0}\sinh(\phi)}{\psi}\right) \tag{A6}$$

where

$$\begin{aligned} D_{tot} = {} & \lambda^2\tilde{J}\mathrm{e}^{\tilde{\eta}_0}\left(\lambda\tilde{J}A + BC\right)\left(\exp\left(\frac{B}{\lambda\tilde{J}}\right) - 1\right) \\ & + \left((\mathrm{i}\tilde{\omega} + \mathrm{e}^{\tilde{\eta}_0})\lambda - \mathrm{e}^{\tilde{\eta}_0}/2\right)B^3\cosh(\phi) \\ & - \lambda\mathrm{e}^{\tilde{\eta}_0}B\left(\lambda\tilde{J}A + B\,(A/2 + C)\right) \end{aligned} \tag{A7}$$

and the coefficients A, B, and C are given by

$$A = \frac{\psi\mathrm{e}^{\tilde{\eta}_0}}{\lambda\cosh(\phi)\left(\psi + \mathrm{e}^{\tilde{\eta}_0}\tanh(\phi)\right)} \tag{A8}$$

$$B = -\mathrm{i}\tilde{\omega}\xi^2 - \psi\tanh(\phi) - \frac{\lambda A}{\cosh(\phi)} \tag{A9}$$

$$C = -\frac{\psi\left(\mathrm{i}\tilde{\omega} + \mathrm{e}^{\tilde{\eta}_0}\right)}{\cosh(\phi)\left(\psi + \mathrm{e}^{\tilde{\eta}_0}\tanh(\phi)\right)} \tag{A10}$$

Auxiliary parameters ϕ and ξ are given by

$$\begin{aligned} \phi &= \mu\tilde{l}_b\sqrt{\mathrm{i}\tilde{\omega}/\tilde{D}_b} \\ \psi &= \mu\sqrt{\mathrm{i}\tilde{\omega}\tilde{D}_b} \end{aligned} \tag{A11}$$

- The cell polarization curve is

$$\mathrm{e}^{\tilde{\eta}_0} = -\lambda\ln\left(1 - \frac{1}{\lambda}\right)\tilde{J} \tag{A12}$$

- GDL R_{gdl}, faradaic R_f, and channel R_{chan} resistivities in the dimension form (Ω cm^2):

$$\begin{aligned} R_{gdl} &= \frac{bl_b}{4FD_b c_h^{in}}, \\ R_f &= \frac{b}{J} \\ R_h &= -\frac{b}{J}\left(\frac{2}{(2\lambda-1)\ln(1-1/\lambda)} - \lambda\ln\left(1 - \frac{1}{\lambda}\right)\right). \end{aligned} \tag{A13}$$

NOMENCLATURE

$\tilde{}$ marks dimensionless variables

b ORR Tafel slope, V

C_{dl} double-layer volumetric capacitance, F cm^{-3}

c_1 oxygen molar concentration at the CCL/GDL interface, mol cm^{-3}

c_b oxygen molar concentration in the GDL, mol cm^{-3}

c_h oxygen molar concentration in the channel, mol cm^{-3}

c_h^{in} reference (inlet) oxygen concentration, mol cm^{-3}

D_b oxygen diffusion coefficient in the GDL, cm^2 s^{-1}

F Faraday constant, C mol^{-1}

f characteristic frequency, Hz

i_* ORR volumetric exchange current density, A cm^{-3}

i imaginary unit

j local proton current density along the CCL, A cm^{-2}

j_0 local cell current density, A cm^{-2}

l_b GDL thickness, cm

l_t CCL thickness, cm

t time, s

t_* characteristic time, s, **Eq. 9**

x coordinate through the cell, cm

Z local impedance, ohm cm^2

Z_{gdlc} GDL + channel impedance, ohm cm^2

Z_{tot} total cathode side impedance, including faradaic one, ohm cm^2

z coordinate along the cathode channel, cm

Subscripts

0 membrane/CCL interface

1 CCL/GDL interfacesmall-amplitude perturbation

b in the GDL

gdl GDL

$gdlc$ GDL + channel

f characteristic frequency, Hzfaradaic

h air channel

W Warburg

Superscripts

0 membrane/CCL interfacesteady-state value

1 CCL/GDL interfacesmall-amplitude perturbation

Greek

η ORR overpotential, positive by convention, V

λ air flow stoichiometry, **Appendix Eq. A4**

λ_T Tikhonov regularization parameter

μ dimensionless parameter, **Eq. 11**

ξ dimensionless parameter, **Appendix Eq. A4**

ϕ dimensionless parameter. **Appendix Eq. A11**

ψ dimensionless parameter. **Appendix Eq. A11**

ω angular frequency of the AC signal, s^{-1}